13th International Symposium on Particle Image Velocimetry – ISPIV 2019
Munich, Germany, July 22-24, 2019

Comparison of momentum and impulse methods of force estimation using PIV data

Eric Limacher[1*], Jeffrey McClure[2], Serhiy Yarusevych[2], Chris Morton[1]

[1] University of Calgary, Mechanical and Manufacturing Engineering, Calgary, Canada

[2] University of Waterloo, Mechanical and Mechatronics Engineering, Waterloo, Canada

[*] ejlimach@ucalgary.ca

Abstract

The PIV-based estimation of fluid induced loads is investigated using momentum- and impulse-based control volume methods, which require additional calculations of pressure and vorticity surrounding the immersed body, respectively. The methods are evaluated using two flow configurations: a cross-flow over circular cylinder subjected to constant free-stream velocity, and a cylinder accelerating from rest in quiescent fluid. The effects of random error, finite spatio-temporal resolution, and vorticity crossing control volume boundaries are investigated using synthetic PIV data sets from a numerical solution of flow around a circular cylinder at Re = 150. In general, the impulse method yields greater errors than the momentum method, except for estimates of drag at coarse spatial resolution, for which the momentum method generates significant bias errors. When applied to experimental PIV data of an accelerating cylinder in quiescent fluid, high correspondence between the two methods and with reference force balance measurements is observed when appropriate filtering is employed to eliminate high-frequency fluctuations in the force signal.

1 Introduction

As particle image velocimetry (PIV) data have become widely available, the prospect of using these data to estimate force has attracted a great deal of research attention, e.g. (Noca et al., 1999; van Oudheusden et al., 2006; Mohebbian and Rival, 2012; Limacher et al., 2019). Methods of force estimation using PIV data can be organized into two broad categories: momentum methods and impulse methods (Rival and van Oudheusden, 2017). Momentum methods require pressure information to be explicitly evaluated, while impulse methods instead require the evaluation of vorticity. In the present work, one method from each of these categories are compared in their ability to accurately extract force estimates from two-dimensional velocity field data, using both numerical data and a PIV dataset.

The conservation of momentum for a stationary, non-deforming CV encompassing a stationary cylinder leads to the following equation for the fluid force:

$$\mathbf{F} = -\frac{d}{dt}\left(\int_V \rho\mathbf{u}dV\right) - \int_S \rho\mathbf{u}(\mathbf{u}\cdot\hat{\mathbf{n}})dS - \int_S p\hat{\mathbf{n}}dS + \int_S (\boldsymbol{\tau}\cdot\hat{\mathbf{n}})dS \tag{1}$$

where V denotes the fluid volume, S denotes the outer boundary of V, $\hat{\mathbf{n}}$ denotes the outward-facing normal on S, and $\boldsymbol{\tau}$ is the viscous stress tensor (Rival and van Oudheusden, 2017). $\mathbf{F}$ is the instantaneous fluid force acting on the cylinder, $\mathbf{u}$ is the velocity and p is the pressure.

For a stationary body in a stationary, non-deforming CV, the impulse force formulation is given as

$$\mathbf{F} = -\rho\frac{d}{dt}\int_V \mathbf{x}\times\boldsymbol{\omega}dV - \rho\oint_S (\hat{\mathbf{n}}\cdot\mathbf{u})(\mathbf{x}\times\boldsymbol{\omega})dS + \rho\oint_S\left(\frac{1}{2}\hat{\mathbf{n}}u^2 - (\hat{\mathbf{n}}\cdot\mathbf{u})\mathbf{u}\right)dS + \mu\oint_S\left(\mathbf{x}\times\frac{\partial\boldsymbol{\omega}}{\partial n} - \hat{\mathbf{n}}\times\boldsymbol{\omega}\right)dS, \quad (2)$$

where $\mathbf{x}$ is the position vector relative to the centre of the cylinder. The first term on the right-hand side is the rate of change of vortical impulse within the domain, and the second term is the net flux of impulse out from the domain, jointly representing the material derivative of impulse in V. The remaining two integrals jointly account for the material derivative of impulse in the unobserved domain external to V. In two dimensions, the general force expression given in Kang et al. (2017) is equivalent to equation (2).

In the present study, discretized versions of equations (1) and (2) are applied to two test cases: (i) data from a numerical simulation of the flow around a two-dimensional circular cylinder (of diameter D) in a steady freestream (U_∞) at a Reynolds number of 150, and (ii) data from a PIV experiment of an accelerating cylinder in quiescent fluid at a peak Reynolds number of approximately 5100 (Limacher et al., 2019). The first test case was considered to facilitate a comparative analysis of the sensitivity of the two methods to random errors and to spatio-temporal resolutions representative of PIV data, while the the second test case provides an experimental comparison basis using a different flow scenario. The numerical solution was interpolated onto a square Cartesian grid where synthetically generated random errors are added to the velocity fields to mimic PIV datasets. Details on the discretization of equations (1) and (2) are given in section 2, while the numerical and experimental results are presented in section 3 and 4, respectively.

2 Discretization of momentum and impulse equations

For the impulse formulation, second-order central differencing schemes are used for spatial and temporal derivatives. For both methods, trapezoidal integration along each segment of the contour S is employed, and midpoint integration is employed for the area integral. In the impulse method, to avoid over-estimating the contribution of data points adjacent to the contour S, the contour is defined to lie halfway between the grid points used in the area integral. Data points on the contour are then linearly interpolated from the adjacent grid points. In the momentum formulations, the contours defining the control volume are chosen to lie on grid points, and the contribution to the area integral by the boundary points is truncated instead.

For the momentum formulations, the pressure field (p) is estimated from the discretized velocity field and its derivatives by solving the Poisson equation with boundary conditions and source terms computed from the PIV data (van Oudheusden, 2013). Since different boundary conditions exhibit different sensitivities to experimental error (Pan et al., 2016), two versions will be compared herein: the Neumann case,where Neumann boundary conditions are employed on all the cylinder and domain boundaries, and the Dirichlet case, where Neumann conditions are employed on the cylinder, upstream and downstream boundary conditions, and Dirichlet boundary conditions are employed on the top and bottom domain boundaries. For the Dirichlet condition, the pressure on the boundary is set using an extended form of the Bernoulli equation, valid for unsteady, irrotational flow with small mean velocity gradients (de Kat and van Oudheusden, 2012). The Laplacian of the pressure field is discretized using a 5-point second-order central difference scheme, which entails the use of "ghost grid points" at the boundaries (McClure and Yarusevych, 2017b).

As will be demonstrated later, errors in the impulse-based force estimates are exacerbated by the presence of vorticity on the outer control surface. As a result, two versions of the impulse formulation are presented: one with a static CV, and one with a dynamic CV wherein the downstream plane location, x_D^*, is selected at each instant in time to minimize the integral of enstrophy on S. Since equation (2) is valid only for a static CV, the force at each instant for the dynamic CV method must be calculated from a series of three data points to permit the approximation of the time derivative of impulse by central differencing. For the numerical data, the domain of possible downstream plane locations is $x_D^* \in [5,9]$. The downstream extent of this domain, though likely inconvenient to resolve in PIV investigations, is employed here to demonstrate the possibility of error reduction. The control volumes employed for the different methodologies are listed in table 1.

3 Numerical Investigation

3.1 CFD Methodology

The software Fluent 15.0 was used to complete a laminar simulation of the unsteady flow around a two-dimensional circular cylinder at a Reynolds number of $Re = \rho U_\infty D/\mu = 150$. A finite-volume approach was used, employing the SIMPLE algorithm (Versteeg and Malalasekera, 2007) to solve the continuity and Navier-Stokes equations for incompressible flow. The employed spatial discretization schemes are as follows: least-squares cell-based for gradient, second-order for pressure, and second-order upwind for momentum. Temporal discretization was achieved using a second-order implicit transient scheme. A constant velocity boundary condition was specified on the upstream face, and an outflow boundary condition was specified on the downstream plane. The no-slip and impermeable boundaries were imposed at the cylinder surface, and the lateral outer domain boundaries were specified as impermeable but with zero shear. The calculation domain extended 20 diameters upstream, 30 diameters downstream, and 20 diameters to either side of the cylinder. The resulting computational grid is over 1.7 million nodes. A constant time step of $\Delta t = 0.005$s was used, resulting in a maximum Courant number ($Co = u\Delta t/\Delta x$) of just over 5. The solution was run until the formation of a stable vortex street was observed and the mean drag and root-mean-square (RMS) lift coefficients had reached an acceptable level of convergence.

3.2 Synthetic PIV Error and Parameter Space

The numerical solution data were interpolated onto a square Cartesian grid of $\Delta x/D = h^* = 0.01$ and at a time separation of $\Delta t D/U_\infty = \Delta t^* = 0.075$. Spatial and temporal resolutions were then varied by under-sampling the data (Table 2), spanning $0.01 < h^* < 0.1$ in space and $0.075 < \Delta t^* < 0.3$ in time.

To quantify the sensitivity of the force estimations to random measurement errors, synthetic random errors were added to the sampled velocity fields representative of those typically encountered in PIV experiments. Figure 1a shows a single instantaneous realization of the generated streamwise velocity error for a spatial resolution of $h^* = 0.02$, and figure 1b shows the corresponding instantaneous vorticity field with the generated errors. The standard deviation of the error at a given spatial location and time is prescribed following McClure and Yarusevych (2017a). A standard deviation of 0.5% of the maximum velocity ($\approx 1.4U_\infty$) is prescribed globally to model random errors in correlation peak identification in PIV measurement. To model PIV errors in highly sheared regions, a standard deviation of up to 7.5% of the maximum velocity is prescribed based on the local magnitude of the velocity gradient tensor; by keeping this value constant for all cases, it is assumed that the seeding density is constant (Howell, 2018). The prescription of a constant global error level, rather than a more general relation coupled to the spatial and time scales of the PIV acquisition, is justified if it is assumed the experimentalist chooses the pulse separation to maintain a constant freestream particle displacement between pulses. The selected 0.5% error corresponds to a 0.06px peak detection error when the maximum particle displacement is half of a 24×24px interrogation window. This places a lower bound on the time separations in which the constant free-stream error assumption is valid, since the time separation between vector fields cannot be less than the pulse separation. Hence, random-error sensitivity of the force estimation methods is only studied for cases where $\Delta t^*/4h^* > 0.5$ (see table 2). To model the spatial correlation of PIV errors due to an interrogation window overlap of 75% (Sciacchitano and Wieneke, 2016), the uncorrelated random error field generated at each instant is convolved with a 7×7 matrix that results in a positive autocorrelation of the errors, decreasing linearly with spatial separation for spatial separations less than one interrogation window width.

Methodology	**CV definition**: $[x^*_{\min}, x^*_{\max}, y^*_{\min}, y^*_{\max}]$
momentum, Dirichlet BC:	$[-1,\ 1,\ -1,\ 1]$
momentum, Neumann BC:	$[-1,\ 1,\ -1,\ 1]$
impulse, static CV:	$[-1,\ 5,\ -2.4,\ 2.4] + 0.5h^*[-1,\ 1,\ -1,\ 1]$
impulse, dynamic CV:	$[-1,\ x^*_D,\ -2.4,\ 2.4] + 0.5h^*[-1,\ 0,\ -1,\ 1]$

Table 1: Control volume definitions for various methods. The location of the downstream face, $x^*_D \in [5,9]$, varies in the dynamic CV definition so as to minimize the integral of enstrophy on S.

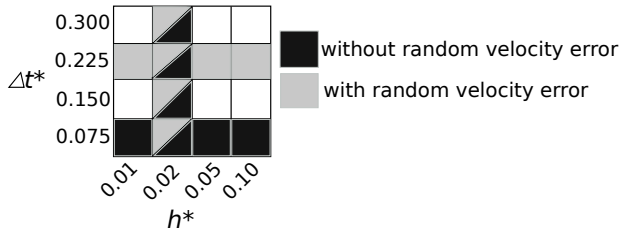

Table 2: Parameter space of spatial and temporal resolutions investigated using the CFD results.

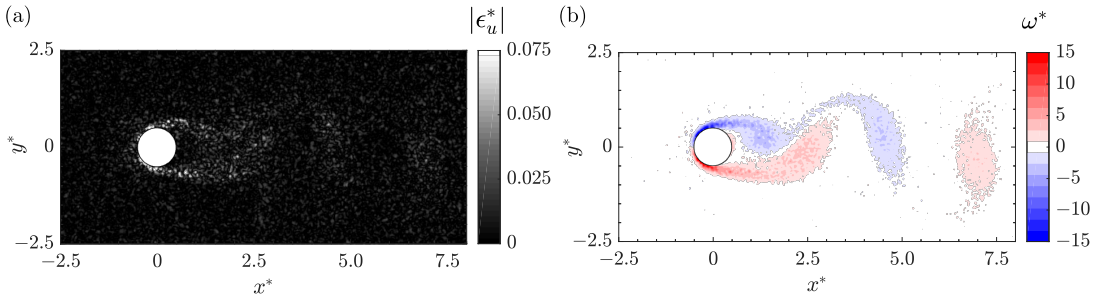

Figure 1: Example of the synthetic random error applied to the sampled cylinder flow velocity data: (a) instantaneous magnitude of the streamwise velocity error, (b) instantaneous vorticity field with errors.

3.3 Numerical Results

Force coefficient estimates are reported using the subscripts *mom* and *imp* to refer to the momentum and impulse formulations, with the additional subscripts *Neu* and *Dir* to denote the two alternative boundary conditions used in the momentum method. The additional subscript *dyn* refers to the variation of the impulse method in which the CV is varied in time to minimize enstrophy on S. The subscript CFD refers to force coefficients obtained directly from integration of the stresses on the cylinder. The instantaneous lift and drag are normalized by $1/2\rho DU_\infty^2$ to yield lift and drag coefficients C_L and C_D, respectively.

Figure 2 plots the results of each of the force estimation methods for the finest spatial and temporal resolutions available, that is, $h^* = 0.01$ and $\Delta t^* = 0.075$, without random error added to the velocity fields. The impulse method with a static CV exhibits periodic errors in both lift and drag relative to the CFD results. The occurrences of greatest instantaneous error are correlated with vortices crossing the contour S. When vorticity is avoided by using a dynamic CV definition, in which the downstream face tends to convect with the wake, instantaneous errors are greatly reduced. The remaining erroneous spikes in $C_{D,imp,dyn}$ and $C_{L,imp,dyn}$ occur when the downstream face (containing the lowest enstrophy) reaches the limits of the permissible domain and then discontinuously jumps to an upstream spatial location. The momentum method exhibits low error in lift and drag, with a minor bias error in drag estimates. Given the use of a Neumann boundary condition on the downstream wake plane, the momentum method is not affected by the presence of vorticity on the outer contour.

Root-mean-square (RMS) errors in the drag and lift coefficients, ε_D^{RMS} and ε_L^{RMS}, are calculated over two complete shedding cycles. Figure 3 shows the RMS errors for each method, identified by the earlier defined subscripts, for the combinations of spatial and temporal resolutions studied. The momentum method yields lower RMS errors than the impulse method for all cases other than for drag at coarse spatial resolutions, i.e. $h^* \geq 0.05$ (figure 3a). For the impulse method, the use of a dynamic CV reduces the RMS errors to levels similar to the momentum method, except for the two coarsest temporal resolutions where more pronounced deviations are observed in the lift data (figure 3d).

Interestingly, the impulse method exhibits minima in the RMS error for both drag and lift at a spatial resolution of $h^* = 0.05$ in figures 3a and 3b. The authors speculate that this minimum is explained by the interaction between the impulse-derivative and impulse-flux terms (the first two terms on the right-hand side of equation (2)). The combination of these two terms represents the material derivative of impulse in

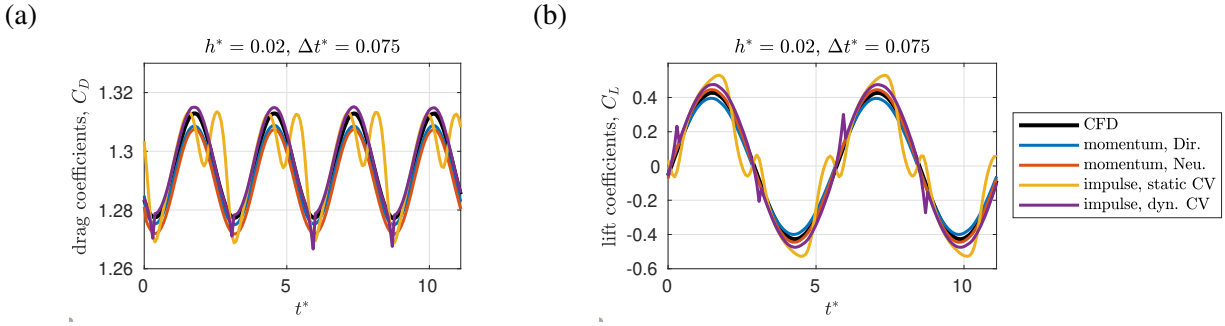

Figure 2: Force coefficients for the finest resolution case: $h^* = 0.01$, $\Delta t^* = 0.075$; (a) drag coefficients; (b) lift coefficients.

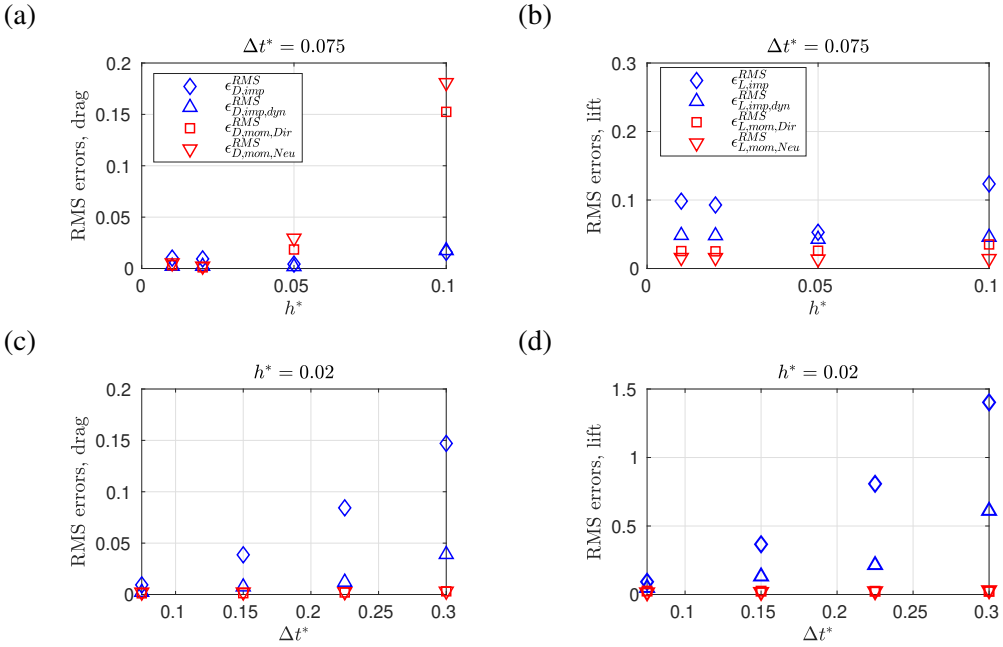

Figure 3: RMS errors for each of the force estimation methods for varied temporal and spatial resolutions. (a,b) constant temporal resolution $\Delta t^* = 0.075$, varied spatial resolution; (c,d) constant spatial resolution $h^* = 0.02$, varied temporal resolution. Drag coefficients are on the left, lift coefficients are on the right.

V, which, though relatively small, is evaluated as the difference of two relatively large integral quantities. Moderate coarsening of the spatial resolution yields an artificial reduction in the evaluated vorticity, which can reduce the error in the material derivative of impulse. As h^* continues to increase, truncation errors in the approximated spatial derivative begin to dominate.

Figure 4 presents the calculated lift and drag coefficients, without random error added to the velocity fields, at varied spatial resolution at a constant temporal resolution of $\Delta t^* = 0.075$. The errors for the static-CV impulse method are of near-zero mean, but are not negligible instantaneously (see figures 4a and 4b). The use of a dynamic CV significantly reduces the instantaneous errors, leaving minor erroneous spikes where the CV discontinuously jumps upstream (figures 4c and 4d). A bias in the drag coefficients for the momentum method, which grows as the spatial resolution coarsens (figure 4e), is found to be the cause of the higher RMS errors seen in figure 3a; however, the lift estimates are not affected significantly by increasing h^* (figure 4f). Visibly, these trends are nearly identical for both the Dirchlet and Neumann boundary conditions, so the latter has been omitted from figure 4 for brevity.

The impulse method is highly sensitive to the coarsening of the temporal resolution (figures 3c and 3d). As

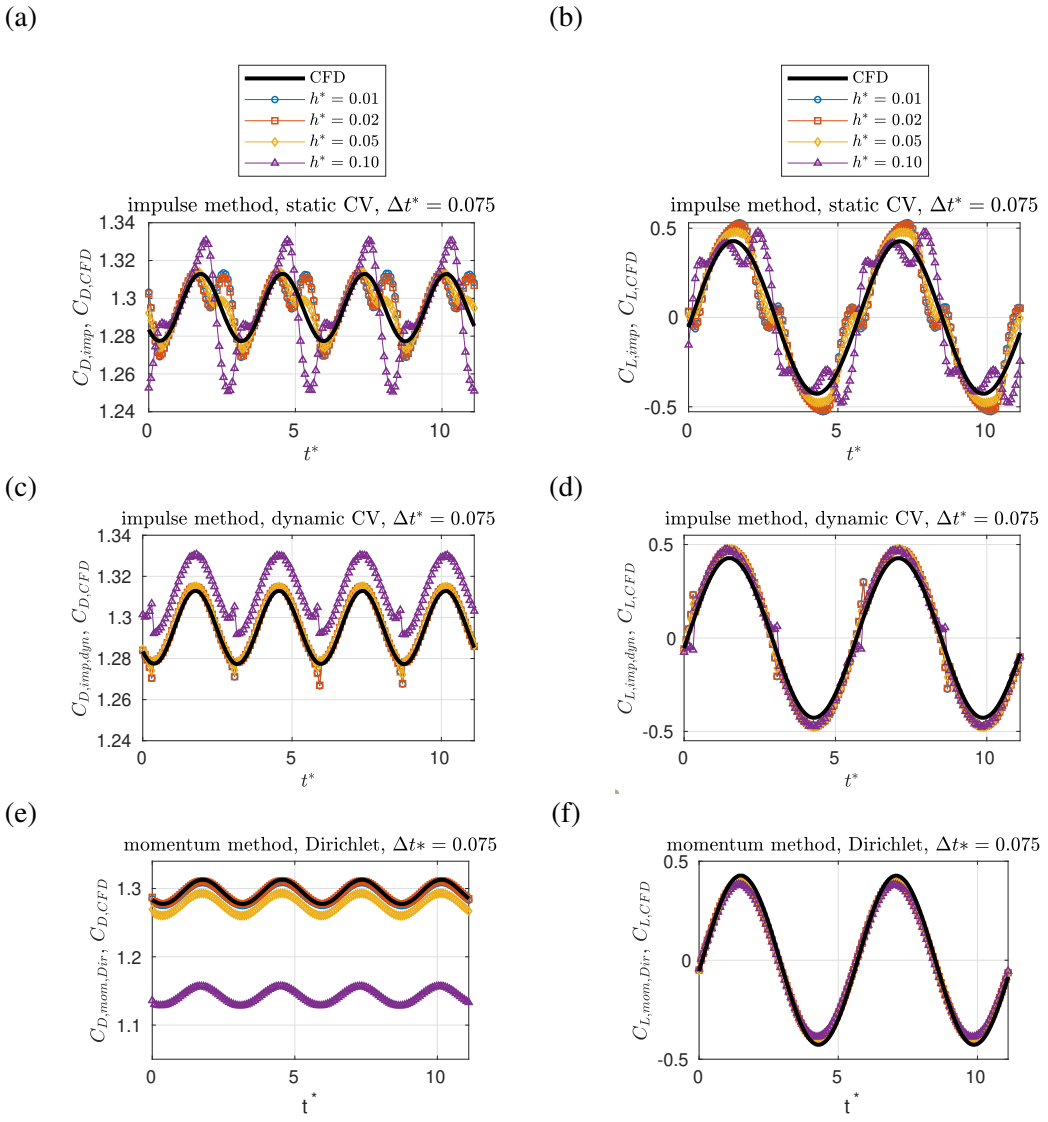

Figure 4: Effect of spatial resolution on force estimates for the various methods at a fixed temporal resolution of $\Delta t^* = 0.075$. (a,b) impulse method for a static CV; (c,d)impulse method for a dynamic CV; (e,f) momentum method with Dirchlet BC.

Δt^* increases, the vortical structures in the wake travel an increasing fraction of a cylinder diameter between vector fields, increasing truncation error in the approximated time derivative of impulse. Contrary to the fine temporal resolution cases, the dynamic CV method fails to bring the errors down to a similar magnitude as the momentum method for the greater Δt^* cases. In comparison, the two momentum method variants both agree with the CFD forces very well and exhibit only minor variation for the range of temporal resolutions presented here.

For the case of $h^* = 0.02$ and $\Delta t^* = 0.075$, figure 5 shows the estimated forces for the momentum method and the static-CV impulse method after correlated random error has been added to the velocity fields. The instantaneous error for the impulse method is consistently an order of magnitude greater than the momentum method. The errors are manifested in high-frequency content, suggesting that the time derivative in the first term of equation (2) has amplified the random error in the impulse integral. Since these errors remain of near-zero mean, it is plausible that they could be filtered in cases with sufficient temporal resolution.

Figure 6 shows the RMS errors in drag and lift coefficients for the momentum and impulse methods after

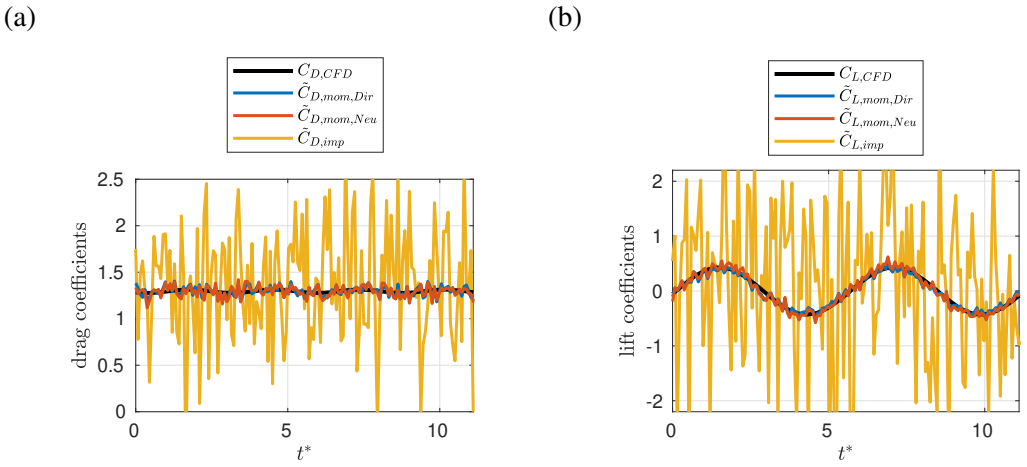

Figure 5: Comparison of momentum and impulse based force estimates with correlated random error added to the velocity fields; (a) drag coefficients, $\tilde{C}_{D,(\cdot)}$; (b) lift coefficients, $\tilde{C}_{L,(\cdot)}$.

adding random error to the velocity fields. In these plots, RMS error is defined with respect to the previously obtained force estimates, indicating how error is increased by the presence of random velocity error rather than reporting total absolute error relative to the CFD results. RMS errors and force coefficients defined in this way are denoted by the tilde symbol, e.g. $\tilde{\varepsilon}^{RMS}_{D,imp}$. Both variants of the momentum method are insensitive to changes in temporal resolution, with only a slight decrease in error with increasing Δt^*. When h^* is varied in figures 6a and 6b, the minima at $h^* = 0.02$ suggest that random error propagation through the momentum force formulation becomes more significant as h^* decreases. On the other hand, truncation error propagation through the force formulation is dominant for $h^* \geq 0.05$. The impulse method exhibits a minimum in RMS error with respect to both spatial and temporal resolutions (figures 6c, 6d, 6e and 6). As noted previously for the cases without random velocity error, the minima with respect to h^* in figures 6c and 6d can be explained in terms of reduced error in the sum of the impulse-derivative and impulse-flux terms. The minima with respect to Δt^* in figures 6g and 6h can be explained by two competing factors; the amplification of random error through the impulse time derivative decreases as Δt^* increases, but the presence of erroneous vorticity on the outer contour increasingly exacerbates error in the sum of the impulse-derivative and impulse-flux terms as Δt^* increases.

4 Experimental Investigation

4.1 Experimental Methodology

The PIV dataset used in the present investigation is taken from the work of Limacher et al. (2019), which may be consulted for further experimental details. One trial from the highest acceleration case of that work is considered. The cylinder was towed through quiescent water with a triangular acceleration profile, with a peak dimensionless acceleration of $a_p^* = a_p D/U_{\max}^2 = 1$, where a_p is the peak instantaneous acceleration, and a Reynolds number of approximately 5100 at the maximum cylinder velocity.

4.2 Experimental Results

Both force estimation methods utilize a control volume that is fixed relative to the cylinder. During the time interval investigated, no vorticity crosses the domain boundaries, allowing all of the contour integrals in the impulse formulation to be omitted. The acceleration of the cylinder requires the addition of another term:

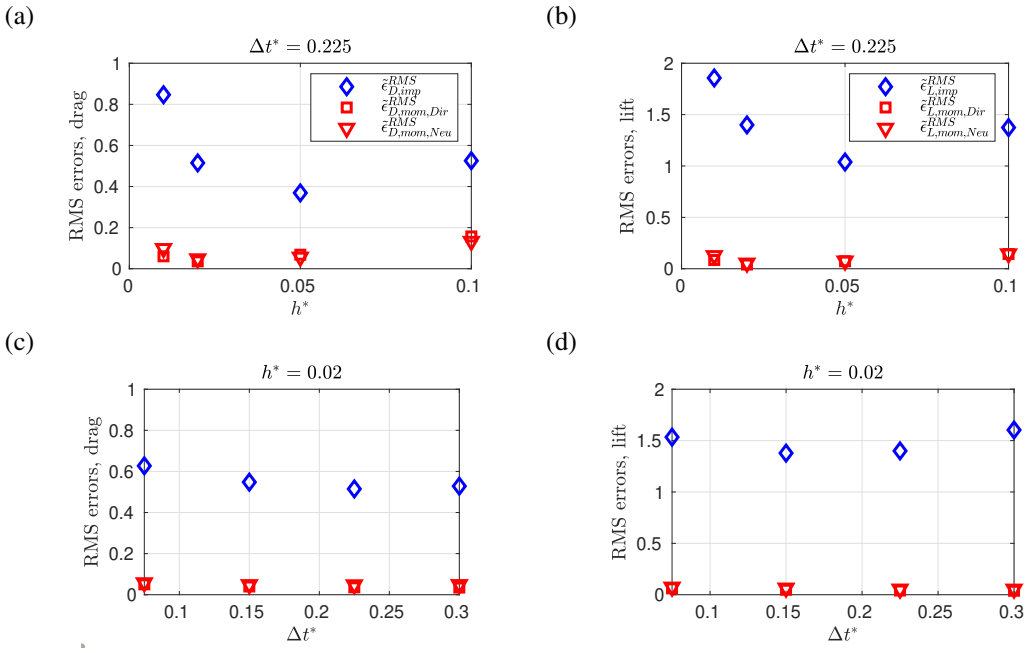

Figure 6: RMS errors in drag coefficients (left) and lift coefficients (right) with correlated random error added to the velocity fields; (a,b) variable h^*, constant $\Delta t^* = 0.225$; (c,d) variable Δt^*, constant $h^* = 0.02$.

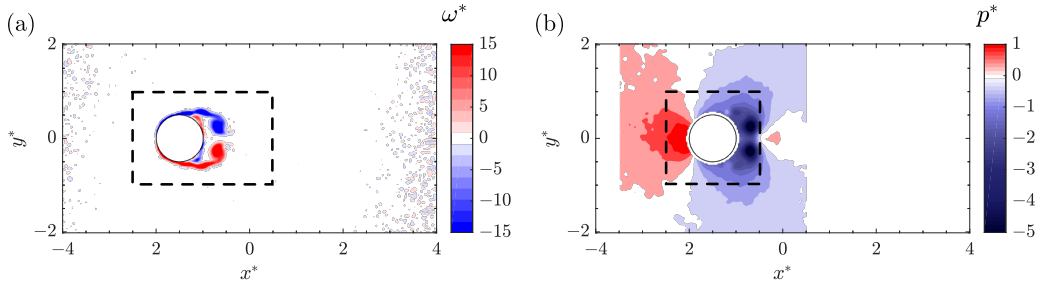

Figure 7: (a) Vorticity field with impulse formulation CV indicated with a black dashed line at $t^* = 3.5$ and (b) pressure field with momentum formulation CV indicated with a black dashed line at $t^* = 3.5$

$$\mathbf{F} = -\rho \frac{d}{dt} \int_V \mathbf{x} \times \boldsymbol{\omega} dV + \rho V_b \frac{du_c}{dt}, \tag{3}$$

where du_c/dt is the cylinder acceleration, defined here to be positive, and V_b is the body volume (Limacher et al., 2019). This term is distinct from the classical added-mass force, since it lends a force in the *same* direction as the acceleration, not in opposition to it. Figure 7a shows an instantaneous vorticity field derived from the PIV measurements at $t^* = 3.5$, with the black dashed line denoting the boundary of the control volume used to compute the vorticity impulse terms ($-1 < x^* < 2$, $-1 < y^* < 1$), while figure 7b shows an instantaneous pressure field computed from the Poisson equation with all Neumann boundary conditions, with the black dashed line denoting the boundary of the control volume used to compute the momentum balance ($-1 < x^* < 1$, $-1 < y^* < 1$). The Poisson equation is solved on a domain of $-2 < x^* < 2$, $-2 < y^* < 2$, and the Neumann boundary condition near the cylinder surface is applied on a larger circle of radius $r/D = 0.55$, in order to avoid boundary condition errors associated with computing temporal derivatives near the moving cylinder surface. Since the contribution of pressure to the momentum balance is only through integration along the outer contour of the CV (equation 1), the force estimate is insensitive to position of the inner Poisson equation boundary condition.

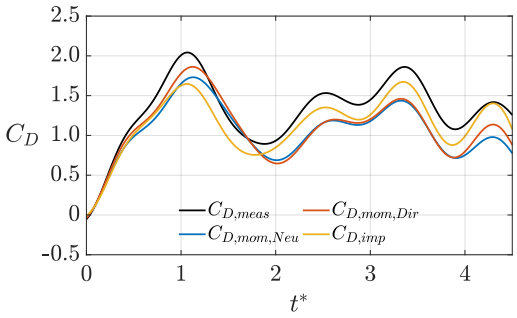

Figure 8: Comparison of filtered force estimates for the accelerating cylinder experiment with filtered force balance data ($C_{D,meas}$).

The force estimations from the impulse and momentum formulations are compared to experimental force-balance data in figure 8. The compared data are low-pass filtered to remove frequencies associated with resonance vibrations of the model, which contaminate the transient measurements. The results of all methods produce signals that, once filtered, have high correspondence to the reference force balance measurements. The force estimates resolve the large initial peak in the force history during the cylinder's acceleration phase. Both methodologies underpredict the drag force slightly, but their fluctuations exhibit high temporal correlation. This underprediction is more pronounced for the momentum formulation at $t^* \geq 2$; this is attributed to the effect of finite spatial resolution on the Poisson pressure solution, resulting in an under prediction of pressure extremes in the stagnation region and low pressure wake vortices (de Kat and van Oudheusden, 2012). For the impulse formulation, the finite resolution of the PIV data may lead to an under prediction of the viscous drag component associated with computing the vorticity near the cylinder surface Limacher et al. (2019), although this requires further quantification.

5 Conclusions

A comparative analysis of two methods of estimating force from two-dimensional velocity data – one based on momentum, one based on impulse – was carried out in the present work. The comparison considered the effects of spatial resolution, temporal resolution and random velocity error.

The impulse method was found to be highly sensitive to changes in temporal resolution. It is clear that Δt^* must be kept below some characteristic time scale to limit the convection of vortical structures between time steps, so as to limit truncation error in the approximated time derivative of impulse. By contrast, the momentum method, using either Neumann or Dirchlet boundary conditions for the Poisson pressure solver, exhibited low RMS errors for all tested temporal resolutions at a fixed spatial resolution of $h^* = 0.02$ for both drag and lift.

The greatest instantaneous errors in the impulse formulation occur when vorticity is crossing the control surface. This source of this error is related to the attempt to calculate a small difference between two large quantities: the rate of change of impulse in the domain and the flux of impulse crossing the control surface. The use of a moving wake plane location to minimize instantaneous total enstrophy on the outer contour leads to a substantial reduction in error. However, even for the finest temporal resolutions, this dynamic-CV variant of the impulse method yields slightly higher RMS errors than the corresponding estimates from the momentum method.

Changes in spatial resolution had a less significant effect on the impulse formulation than temporal resolution, with RMS error actually decreasing for the impulse method as spatial resolution was changed from $h^* = 0.01$ to 0.05. This is attributed to the artificial reduction in the calculated values of vorticity, which mitigates the errors associated with vorticity crossing the domain boundary. Lift estimates for the momentum method are insensitive to changes in spatial resolution resolution. However, coarsening of spatial resolution leads to increasingly large underestimates of drag for the momentum method. This bias error is attributed to the underestimation of the pressure extremes in the wake vortices and stagnation region near the leading edge of the cylinder, caused by the spatial filtering of the Poisson equation solution related to the grid resolution. Investigation of this drag-bias issue is a key area of future work for the momentum method.

The impulse formulation showed an order of magnitude greater sensitivity to random velocity error than the momentum formulation. This is attributed to the additional spatial derivative of the velocity field required to calculate vorticity. While the momentum method involves spatial derivatives of the velocity field when solving for pressure, the solution of the Poisson equation itself is equivalent to a spatial integration, thus mitigating error propagation. However, the errors for each method are concentrated at frequencies in the neighbourhood of the sampling frequency, and temporal filtering is recommended for practical use of either methodology. When applied to experimental PIV data with typical levels of random velocity error, low-pass filtering successfully eliminates these high-frequency fluctuations. The filtered results show high correspondence with each other and with reference force balance measurements, although a slight underprediction of drag exists for both methods.

The presented results allow for a recommendation. If one is interested mainly in accurate force estimates, and interest in a specific mode of physical interpretation is secondary, then the presented momentum method is a more robust choice than the impulse method, at least when vorticity is expected to cross the domain boundaries. A key motivation for the continued study of impulse methods is the appealing possibility of attributing force components to the evolution of specific vortical structures. Fortunately, the present work suggests that efforts to identify CVs that enclose such structures are also likely to reduce error by avoiding vorticity on the boundary.

References

de Kat R and van Oudheusden B (2012) Instantaneous planar pressure determination from PIV in turbulent flow. *Exp Fluids* 52:1089–1106

Howell J (2018) *Distribution of Particle Image Velocimetry (PIV) Errors in a Planar Jet*. Ph.D. thesis. Utah State University

Kang L, Liu L, Su W, and Wu J (2017) A minimum-domain impulse theory for unsteady aerodynamic force with discrete wake. *TAML* 7:306–310

Limacher E, Morton C, and Wood D (2019) On the calculation of force from PIV data using the generalized added-mass and circulatory force decomposition. *Exp Fluids* 60:4

McClure J and Yarusevych S (2017a) Instantaneous PIV/PTV-based pressure gradient estimation: a framework for error analysis and correction. *Exp Fluids* 58:92

McClure J and Yarusevych S (2017b) Optimization of planar PIV-based pressure estimates in laminar and turbulent wakes. *Exp Fluids* 58:62

Mohebbian A and Rival DE (2012) Assessment of the derivative-moment transformation method for unsteady-load estimation. *Exp Fluids* 53:319–330

Noca F, Shiels D, and Jeon D (1999) A comparison of methods for evaluating time-dependent fluid dynamic forces on bodies, using only velocity fields and their derivatives. *J. Fluids Struct* 13:551–578

Pan Z, Whitehead J, Thompson S, and Truscott T (2016) Error Propagation Dynamics of PIV-based Pressure Field Calculations: How well does the pressure Poisson solver perform inherently? *Meas Sci Technol* 27:084012

Rival DE and van Oudheusden B (2017) Load-estimation techniques for unsteady incompressible flows. *Exp Fluids* 58:20

Sciacchitano A and Wieneke B (2016) PIV uncertainty propagation. *Meas Sci Technol* 27:084006

van Oudheusden B (2013) PIV-based pressure measurement. *Meas Sci Technol* 24:032001

van Oudheusden BW, Scarano F, and Casimiri EWF (2006) Non-intrusive load characterization of an airfoil using PIV. *Exp Fluids* 40:988–992

Versteeg HK and Malalasekera W (2007) *An Introduction to Computational Fluid Dynamics: The Finite Volume Method*. Pearson Education Limited. 2nd edition